

A Rubidium M_x -magnetometer for Measurements on Solid State Spins

Daniel Arnold,¹ Steven Siegel,¹ Emily Grisanti,¹ Jörg Wrachtrup,^{1,2} and Ilja Gerhardt^{1,2}

¹⁾ *3. Physikalisches Institut and Stuttgart Research Center of Photonic Engineering (SCoPE), Universität Stuttgart, Pfaffenwaldring 57, Stuttgart D-70569, Germany*

²⁾ *Max Planck Institute for Solid State Research, Heisenbergstraße 1, D-70569 Stuttgart, Germany*

(Dated: 1 November 2016)

The detection of environmental magnetic fields is well established by optically pumped atomic magnetometers. Another focus of magnetometry can be the research on magnetic or spin-active solid-state samples. Here we introduce a simple and compact design of a rubidium-based M_x -magnetometer, which allows for hosting solid-state samples. The optical, mechanical and electrical design is reported, as well as simple measurements which introduce the ground-state spin-relaxation time, the signal-to-noise ratio of a measurement, and subsequently the overall sensitivity of the magnetometer. The magnetometer is optimized for the most sensitive operation with respect to laser power, and magnetic field excitation at the Larmor frequency.

I. INTRODUCTION

To date, the detection of magnetic fields at various frequencies and length-scales is an indispensable tool in applied science. Material science¹, geological explorations², and the characterization of biomagnetic fields³ are performed with an accuracy, which was not available some decades ago. Most recently, the combination of magnetometers with nuclear magnetic resonance⁴ and its related imaging techniques are present in every-day applications. Besides these very technical approaches, a number of current research topics provides insight towards novel sensing applications. Another magnetometry related research field is the implementation of high precision tests in fundamental physics⁵.

Early implementations developed from the detection of (macroscopic) electrical currents towards the detection of quantized entities e.g. flux quanta in a superconducting interference device (SQUID). These devices exhibit record sensitivities in the $\text{aT}/\sqrt{\text{Hz}}$ -range at low frequencies and are commercially available. The availability of liquid helium limits their applicability, especially in off-site applications. In the last two decades, the early experiments on atomic vapors⁶ quickly revealed their sensitivity on external magnetic fields and led to optical pumped magnetometers⁷. Current devices reach sensitivities comparable to the mentioned SQUIDS⁸, but have relaxed requirements in terms of cryogenics.

In parallel to the field of optically pumped atomic magnetometers, the research on spin active defects in diamond has emerged. The best researched defect center is the negatively charged nitrogen-vacancy center⁹. It can be conveniently optically prepared and enables the sensing of environmental spins and the implementation of quantum optical primitives. Early experiments on their coupling to other quantum devices have been performed¹⁰.

Optically pumped magnetometers based on atoms can be implemented in a variety of experimental schemes¹¹. In any case, an (external) magnetic field changes the influence on a near-atom-resonant probe beam. Two

fundamental schemes are well established: The M_z -magnetometer, which detects the fingerprint of the Larmor precession of an atomic ensemble by a steady change in intensity on a photo detector. The other scheme is the M_x -magnetometer. It directly measures the Larmor frequency on the optical signal, which is commonly introduced by a 90° -configuration, comprising a pump and a probe beam. Many derived schemes are established in research, often focusing on special frequency ranges, such as SERF (Spin Exchange Relaxation Free) magnetometry⁸ or the implementation of differential measurement schemes, such as the use of balanced detection, which suppresses the common mode laser noise.

In this paper we present the implementation of a simple M_x -magnetometer based on atomic rubidium. The design is adapted from the Fribourg atomic physics group¹². The magnetometer design introduced in this work combines the pump and the probe beam, which makes it easier to handle. Since the future goal is a combination of this magnetometer and a solid-state spin ensemble, the device allows for hosting an experiment with NV-centers. Therefore, the specially tailored cell-design is described and the important parameters such as spin-lifetime and measurements for describing the magnetometry are introduced. And optimization procedure and the resulting sensitivity are presented at the end of the paper.

II. EXPERIMENTAL SETUP

The design criteria for the setup was having an easy implementable design of a rubidium magnetometer with a reproducible sensitivity. One of the advantages of the M_x design is the possibility to allow the detection completely based on alternating currents (AC). This suppresses a number of unwanted noise effects, such as laser power fluctuations, and other sources of $1/f$, and $1/f^2$ -noise.

The common way of implementing an M_x -magnetometer is a configuration with a pump and a probe beam. Another simplified way is to combine both beams and apply the reference B_0 -field in an angle of 45° with respect to a single laser beam.

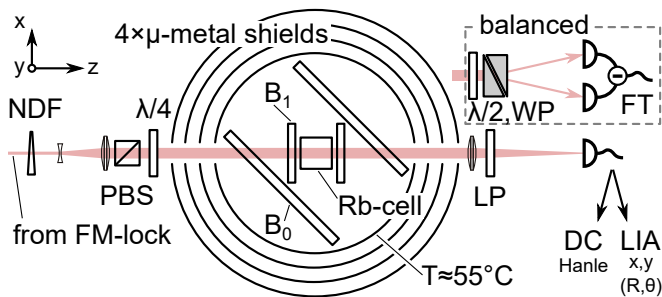


FIG. 1. Experimental setup of the 45° - M_x -magnetometer. A locked laser beam passes a continuously variable neutral density filter (NDF) in order to control the intensity. The beam diameter is increased to $2 \times w_0 = 6$ mm by a concave-convex telescope. The B_0 coils are aligned by 45° with respect to the optical axis, the B_1 coils produce a magnetic field co-linear with the optical path. The (pseudo-)Helmholtz pairs for the compensation of residual fields are not shown. The detectors are placed behind a long-pass filter (LP) and consist either by a normal amplified photo-diode or by balanced detection behind a Wollaston-prism (WP). Signal processing is either performed by a measurement card (DC) or a lock-in amplifier (LIA). The balanced photo-diode signal is processed by a Fourier transformation (FT).

The optical setup of our M_x -magnetometer is shown in Fig. 1. The laser source consists of a commercial Littrow system, operating at approximately 780 nm (DL Pro, Toptica GmbH, Germany). The fiber output of the laser is coupled out and split on a polarizing beam splitter. One part is fed into a Doppler-free frequency modulation rubidium spectroscopy. This allows for a spectral lock, which is performed by a commercial locking system (Digilock, Toptica GmbH, Germany). For the presented experiments, the laser is locked to the D_2 -transition ($5^2S_{1/2} \rightarrow 5^2P_{3/2}$, $F=3 \rightarrow F'=2$). The other part goes to the magnetometry setup. The power can be changed with a neutral density filter wheel, which is calibrated against the input power into the magnetometer. Then the beam is guided upwards to the level of the magnetometry setup (beam height 350 mm) at which point a mirror directs it horizontally towards the μ -metal chambers. On a small platform the beam is widened to approx. 6 mm beam diameter by a telescope. Before entering the measurement setup, the polarization is once more aligned by a polarizing beam splitter and a quarter wave plate to σ^+ -light to pump the atoms in a defined spin polarized state. Behind the magnetometry setup, the continuous beam is focused either on an amplified photo diode (PDA-36A/EC, Thorlabs, US), or alternatively on a balanced detector (Nirvana 2007, Newport, US). To suppress unwanted light, we have introduced a 750 nm long-pass filter, such that even with the lights in the laboratory, no characteristic 50 Hz line frequency is observed by the detector.

The light levels were kept at a minimum, to reduce power broadening effects. A range of the input power from approx. 1 to 600 μ W was measured in front of the magnetometer. The gain of the photo diode was set to

either 30 or 60 dB, depending on the measurement performed.

The signal of the amplified photo diode is analyzed on either a computer based digitizing card (PXI 4462, National Instruments, Austin, TX, US) or fed into a lock-in amplifier (SR 830, Stanford Research, Stanford, CA). The lock-in output (X, Y, or alternatively R, Θ) is again fed into the same measurement card (PXI 4462, National Instruments, Austin, TX, US) as before.

Parallel to this acquisition, the external magnetic fields have to be controlled. This is electrically realized by an analog output card (PXI 6361, National Instruments, Austin, TX, US), which directly drives the B_0 , and B_1 -field. Initial configurations to drive a current in the coils via a dedicated current driver were not required or did not allow for a fine enough resolution. The compensation fields are controlled by a precision power supply (MP2030, Hameg, DE). We use its voltage output in the mV range and verified the validity of Ohm's law by a 6 1/2 digits digital multi meter (PXI 4070, National Instruments, Austin, TX, US).

All cards are locked onto the same PXI internal clock system (10 MHz), such that all samples are concerted with μ s accuracy. All generated and all acquired data are locked to the correct phase of e.g. the alternating B_1 -field.

A self-implemented *Python*-software gives access to a fully remote-controlled measuring operation. The controlled parameters include the laser power, the lock-in amplifier, the photo-diode gain, the compensation coils' power supply, and the heater's temperature. Also, all out- and inputs of the PXI cards are remotely accessible, which are use for data acquisition as well to drive the B_0 - and B_1 -coils. The acquisition program allows for automated measurements based on markup-language based measurement files (YAML). Generally, the photo-diode and/or the lock-in signal is acquired while another parameter is scanned. It is not possible to continuously change the frequency when the lock-in is used due to limitations of the lock-in's internal phase-locked-loop clock to follow an external reference clock source.

The coils are designed to be able to set a static magnetic field in 45° against the optical axis. Additionally, a B_1 -field configuration is collinearly oriented to apply a radio frequency field to the atoms. The design principle is very comparable to earlier works.

For a field compensation, another set of three (pseudo-)Helmholtz coils is introduced. These are shown in Fig. 2. For a complete description of the coil configuration, refer to Tab. I.

The inner sensitive part with all coils and the vapor cell is shielded from the environment by four μ -metal shields (Sekels GmbH, Germany). The inner diameter of the smallest shield is 300 mm. The coils described above are still separated from this shield by at least 30 mm. No further high-frequency suppression, such as Al or Ferrite shielding, is applied. The total shielding setup suppresses external magnetic fields by a factor of 10^6 , according to

coil	R (mm)	d (mm)	N_{win}	R_{Ω} (Ω)	B (mT/A)	ΔB_{\perp} (%)	ΔB_{\parallel} (%)
B_0	90	92	400	2090	3.997	0.00171	0.013
B_1	30	43	25	1820	0.749	0.34928	6.343
B_x	70	72	300	6200	3.854	0.00287	0.074
B_y	120	123	400	6300	2.997	0.00079	0.019
B_z	55	55	200	5150	3.270	0.00038	0.121

TABLE I. Specification of the (pseudo-)Helmholtz coils. Technical properties: R denotes the coil radius and d the distance of the coil pair. N_{win} is the number of windings. R_{Ω} gives the ohmic resistance which consists of the intrinsic resistance of the wire and an additional resistor. Magnetic properties: B gives the magnetic flux for a given current. ΔB_{\perp} and ΔB_{\parallel} is the percentage inhomogeneity of the magnetic flux within the cylindrical probe volume ($\varnothing = 6$ mm, height = 20 mm) induced by one coil pair. ΔB_{\perp} and ΔB_{\parallel} are the perpendicular and parallel components with respect to the laser beam.

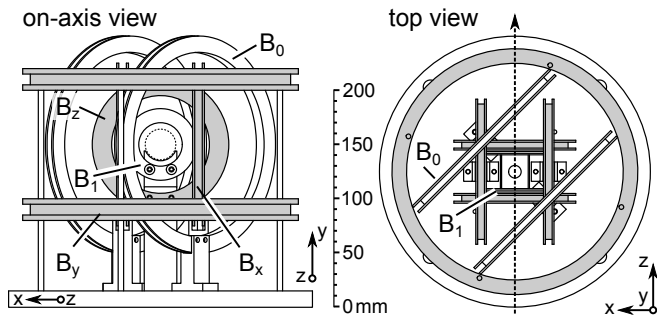


FIG. 2. (Pseudo-)Helmholtz coil configuration for the magnetometer. The coils for the B_0 and B_1 -field are indicated in white. Compensation coils (B_x , B_y , B_z) are indicated in gray. The arrow indicates the optical path. From the bottom (through the holder for the atomic vapor cell) an optical fiber allows for an optical access to a solid-state spin ensemble.

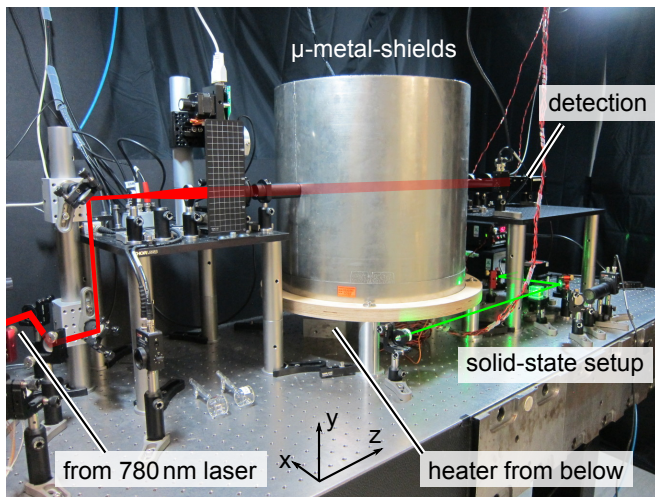


FIG. 3. Optical setup with labeled optical path of the red laser (red) and four mounted μ -metal-shields. The future solid-state spin setup is indicated at the bottom in green, and is optically connected from below the shielding.

the manufacturer.

All shields are vertically mounted on their lids, which are held on the optical table with a wooden support. Five

15 mm holes from the bottom allow for an access from below. These are used for the temperature sensor, the electrical connections to the coils, and the optical and microwave access to the solid-state setup.

The chamber of the inner-most shield is heated by a hot air flow, which is implemented using an SMD-soldering station (Conrad Electronics, Hirschau, Germany) and a supply of compressed air. It is controlled by an external temperature controller (CNPT Series, Omega, Samford, CT, US). The temperature is measured close (50 mm) to the Rb-cell. No influence in the magnetometer signal is observed with and without the temperature sensor. Hot air scintillation is suppressed by 25 mm \varnothing optical borosilicate windows, which are mounted on the most inner shield. In earlier experiments these optical shieldings were not in place and laser power fluctuations were larger. The hot air leaves the shielding via the bottom ports. The temperature of the cells was set to 55°C for all measurements below. This corresponds to an atomic density of 2.24×10^{11} atoms per cm^3 [13].

Special attention was given to the cell design of the magnetometer. Due to our previous experiences in fabricating atomic vapor cells, we kept our common 26 mm inner diameter design and an optical length of the cells of 20 mm. The wall thickness is 2 mm. One of the produced cells is depicted in Fig. 4. It was designed such that it is able to house a tiny solid-state sample and allows for some optical, and electrical access. The atomic probe volume should be close, but eventually inhomogeneously distributed around the sample. All this is realized by a small appendix of the Rb-vapor cell. It is made of 500 μm thick glass tubing with an inner diameter of slightly larger than 2 mm and a length of 10 mm. Optical shielding of the sample against the magnetometer is realized with opaque carbon fiber material. The cell was designed to allow for a beam-diameter of 10 mm. This gives an atomic probe volume of approx. 1600 mm^3 .

Due to the reduced dimension of the cell and the desired sensitivity of the magnetometer, we introduced some measures to increase the spin-relaxation time in the following:

The Rb-reservoir, hosting some solid rubidium, and the cell are mechanically separated. Since solid rubidium in close proximity to the measurement region reduces the

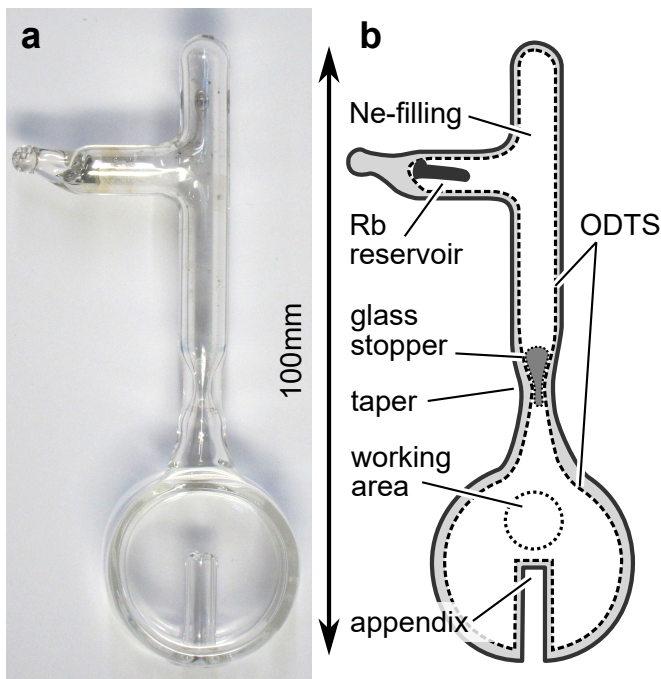


FIG. 4. Front view of a typical Rb-cell. The appendix for the solid-state sample is located at the bottom of the cell. An additional side arm was added for the possibility for opening the glass stem and heating up the horizontal side arm to transfer some rubidium atoms into the cell volume. A glass stopper limits the diffusion of Rb-atoms to the Rb-reservoir. The cell windows are coated with octadecyltrichlorosilane (ODTS), which is used to suppress collisional spin relaxation. 45 torr Ne-buffer gas is added to suppress atom-atom collisions.

spin coherence time, the two compartments of the cell were heated prior to the experiment with a heat gun such that no solid rubidium is in the measurement cell. Note that this procedure takes a long time (approx. 20 hours) because of inhibited diffusion in the cells due to the buffer gas (see below). Afterwards, the cells are homogeneously heated in an oven to the working temperature (approx. 55°C) for 24 hours. Then, a little glass stopper is mechanically brought into place, so that both compartments are separated¹⁴.

One way of increasing the spin relaxation life-time is to suppress diffusion in the cell and to reduce unwanted collisions with the cell walls. Light inert atoms, such as helium or neon, are typically used for this task. Their spin relaxation cross section is low¹⁵. The pressure is calculated by the number of spin relaxing collisions per unit time. For quenching the excited state population, sometimes nitrogen gas is added to the cells. Here we use neon buffer gas since helium tends to diffuse out of the cells. No further nitrogen was added to the cells. The neon pressure for the cell described in this work cell was 45 torr.

Another way of increasing the spin relaxation life-time is coating the walls of the vapor cell with organic compounds such as paraffin^{14,16}. Several different schemes

have been described in literature. Here we use coating with octadecyltrichlorosilane (ODTS, CAS: 112-04-9)¹⁷. The cells were produced by our glass blower’s workshop in such a way that the cell was intact and only the cell stem was open. Then carefully cleaned with the RCA (developed by Radio Corporation of America) standard procedure and dried in an oven at 80°C. A 0.2% solution of ODTS in dried toluene was applied for 48 hours at ambient conditions. The cells were then dried in vacuum, and quickly processed by our glass blower workshop. The ODTS coating is reported to allow for up to 2000 bounces of alkali atoms before they get depolarized. Unlike cells with paraffin coating, these cells are more suitable for higher temperatures. The cells used in the measurements presented in the following aged for about one year.

III. EXPERIMENTAL CHARACTERIZATION

The experimental characterization of the complete magnetometer is divided into the following parts: First the cells are characterized, independently of the exact magnetometry configuration. Then, the ground-state Hanle-resonance¹⁸ occurring at zero magnetic field is used to compensate residual fields inside our measurement configuration¹⁹. Afterwards, non-zero magnetic field measurements are demonstrated. Firstly, the magnetic field is changed and the cell’s achievable linewidth is measured. Secondly, the non-zero magnetic field is kept constant and the achievable signal-to-noise ratio (SNR) is measured. This all comprises the essentials of the magnetometer sensitivity δB .

The cell design as described above might introduce a reduced spin relaxation time due to the appendix, which is very close to the measurement area, that is illuminated by the Rb-resonant laser beam. There are several ways to measure the spin-relaxation time, which utilize more than one beam and perform a pump-probe measurement¹⁴. A simplified measurement with one beam allows for two measurement types performed here. These methods are performed within the magnetometer – but the spin-relaxation time is an intrinsic property of the cell, thus the magnetometer is described in full below.

One way of performing a lifetime measurement is to quickly turn on a magnetic field and observe the system’s coherent response. The atoms start to precess in a coherent fashion after the initial “kick”, but their coherence is lost over time (cf. Fig. 5a) due to spin-relaxation mechanisms like spin-destruction collisions (between alkali- and buffer-gas-atoms and the cell wall), spin-exchange collisions between the alkali-atoms, field gradients across the cell, and interactions with the polarizing light beam²⁰. Usually, the system needs some time to align to the corresponding Larmor frequency. At the end of the relaxation process, the Larmor precession with frequency ω_L is tuned to the magnitude of the external field. No further oscillation, e.g. an external B_1 -field, apart from the initial

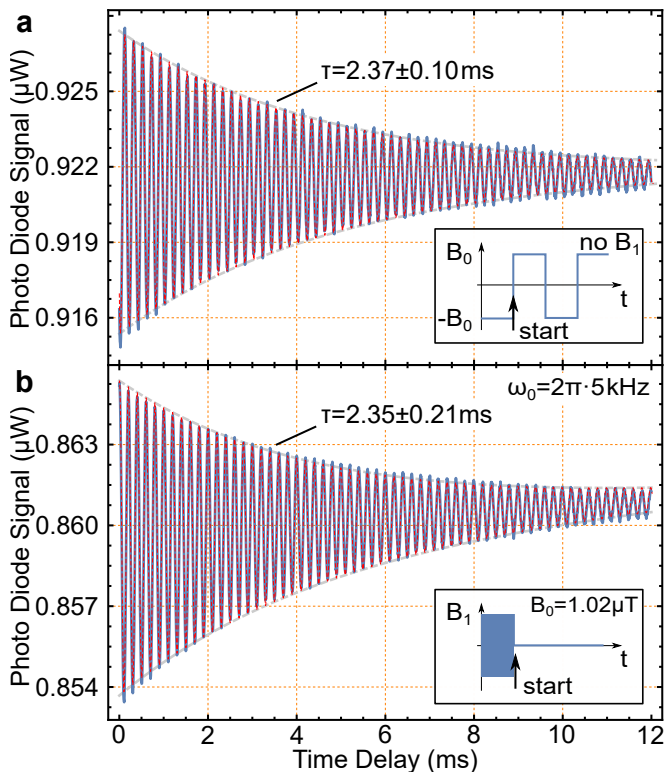


FIG. 5. Lifetime measurements of the spin coherence time at low laser power of 5 μW . (a) The B_0 field is switched on and off. The atomic system starts after the perturbation with some oscillations and the Larmor frequency is reached. The curve is fitted by Eqn. 1 (red dashed line). (b) At a static B_0 -field, corresponding to a Larmor frequency of 5 kHz, the B_1 -field is used to drive the atoms coherently to their Larmor precession. At time zero, the B_1 -field is switched off. Data is fitted by Eqn. 2. The achievable (half-)linewidth (HWHM) of the implemented magnetometer is approx. $1/(2 \times 2\pi\tau) = 34$ Hz.

switch-on, is applied in this scheme. One crucial point is that the transient time to switch on the magnetic field has to be significantly smaller than the relaxation time. The response can be described as a damped oscillator²¹ with some initial transience by assuming an exponential frequency approach where the oscillation converges to the correct Larmor frequency ω_L after a characteristic transient time τ_0 : The response, a damped oscillation with some initial transient, is described by:

$$\xi(t) = a \sin(\omega_L(1 - e^{-\frac{t+t_0}{\tau_0}})t + \varphi)e^{-\frac{t}{2\tau}} + mt + b \quad (1)$$

a denotes the amplitude of the oscillation at time $t = 0$ and φ is its phase. The parameter t_0 determines the initial frequency. Since a positive slope m is inherent in the signal's envelope, a linear term is added. b is the background offset. The switching of the B_0 -field results in an observed characteristic spin-lifetime $\tau = 2.37 \pm 0.10$ ms. This corresponds to an expected natural linewidth (HWHM) of 34 Hz.

Another common way is to align an external magnetic

field (B_0) offset related to a desired Larmor precession and to drive the atoms coherently with a resonant external sinusoidal radio frequency field (rf), that is applied via the B_1 -coils. After the driving field is switched off, the intrinsic Larmor precession decays for the characteristic spin relaxation time. This is shown in Fig. 5b. This case is described by a simple damped oscillator without any time dependence of the frequency:

$$\xi(t) = a \sin(\omega_L t + \varphi)e^{-\frac{t}{2\tau}} + mt + b \quad (2)$$

The resulting lifetime τ of 2.35 ms is compatible with the prior measurement. The cells are now characterized inside the magnetometer configuration.

Although the prior measurements are performed inside our magnetometry configuration, their relevance is independent of the specific implementation of the magnetometer which is introduced now.

After inserting the cells into the magnetometer, an important first step is the compensation of residual fields inside the shielding chamber, since every rearrangement is influencing the remanent magnetization. Since we do not have an option to demagnetize the chamber, we rely on the compensation coils (B_x, B_y, B_z) described above. This is commonly performed by monitoring the Hanle resonance¹⁹, which appears at zero magnetic field. It describes the polarization of the atoms and the orientation of the quantization axis. The height, the sign, and the width are indicators for a correct compensation of the fields.

The procedure to compensate residual fields (based on the set-up introduced above) is as follows:

1. A longitudinal magnetic field (B_z with respect to the laser beam, z -direction) is scanned over zero. Then, the transversal field components (B_x, B_y) are used to minimize the amplitude of the observed Hanle resonance. In the ideal case, the Hanle resonance vanishes.
2. A transversal magnetic field is scanned over zero in the x - or y -direction. The resulting residual field is compensated by adjusting the longitudinal field component in the z -direction.

To verify a successful residual field compensation, the (45° -) B_0 field is scanned spanning over zero magnetic field. Usually, in addition, a magnetic sinusoidal rf B_1 field is applied. As calculated by the magnetic Bloch-equations, the Hanle resonance should point upwards and be centered around the zero field crossing while Larmor resonances corresponding to the B_1 frequency are observed symmetrically around zero (cf. Fig. 6a). An automated compensation process is easily implemented by software.

One crucial parameter of the magnetometer sensitivity is the magnetic resonance linewidth $\Delta\nu_{\text{HWHM}}$ which can easily be obtained by performing a measurement with phase-sensitive detection using a lock-in amplifier which

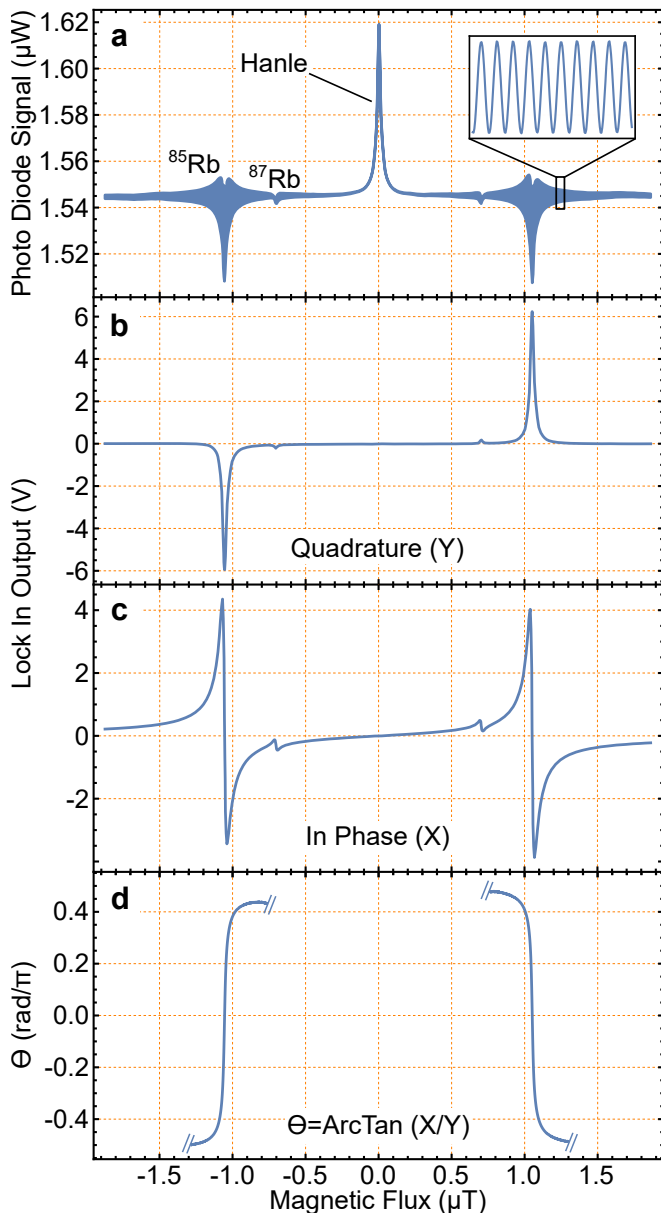


FIG. 6. Raw data of the Rb magnetometer output for the 45° - M_x configuration at a small laser power of $10 \mu\text{W}$ and compensated residual fields. For a fixed B_1 frequency at 5 kHz , the Rb vapor was exposed to a slow B_0 sweep executed over a period of 20 sec. (a) shows the Hanle resonance centered around $B_0 = 0$ and B_1 resonances when B_0 -field corresponds to an atomic transition of the B_1 -Larmor-frequency at 5 kHz . The inset is a zoom into the resonance spike for visualization of the 5 kHz -oscillation. (b) and (c) are the lock-in quadrature (Y) and in phase (X) outputs, respectively, for a lock-in time constant of $100 \mu\text{s}$ and a sensitivity of 20 mV . (d) is the phase signal Θ obtained from the ratio of both lock-in outputs and Eqn. 5.

the photo-diode signal is fed into. To achieve this, a static rf B_1 field and a B_0 field scan across Larmor resonances are applied to the polarized Rb vapor.

We generate a second sine wave with equal frequency

and phase but higher amplitude and use it as a reference signal for the lock-in amplifier. This allows the application of very weak rf B_1 fields since the phase-detection via the lock-in is amplitude limited. Fig. 6b, c, and Fig. 7 show the quadrature output (Y), and the in-phase output (X) of the lock-in amplifier. The width can be extracted by a Lorentzian fit¹² (Eqn. 3) in case of the quadrature, by determining the extrema of the dispersive in-phase output¹² or via a fit of Eqn. 4, where $x = (\nu_L - \nu_{\text{rf}})/\Delta\nu_{\text{HWHM}}$ is the detuning normalized to the (light-power dependent) linewidth $\Delta\nu_{\text{HWHM}}$ of the resonance relating to the rf magnetic B_1 field.

$$Y(x) = -A \frac{x}{x^2 + 1 + S} \quad (3)$$

$$X(x) = -A \frac{1}{x^2 + 1 + S} \quad (4)$$

$$\Theta(x) = \arctan x \quad (5)$$

The broadening of the line due to the power (rms) of the rf field is described by the saturation parameter S . The phase signal $\Theta(x)$, which is determined by the ratio of both lock-in outputs $X(x)/Y(x)$, excludes S . Hence, the width of $\Theta(x)$ in Eqn. 5 is immune to rf power broadening¹². The frequency can be expressed in the magnetic flux B (and vice versa) with $\nu_L = (\gamma/2\pi) \times B$. The rubidium ⁸⁵'s gyromagnetic ratio is $\gamma = 4.7 \text{ Hz/nT}$ [13].

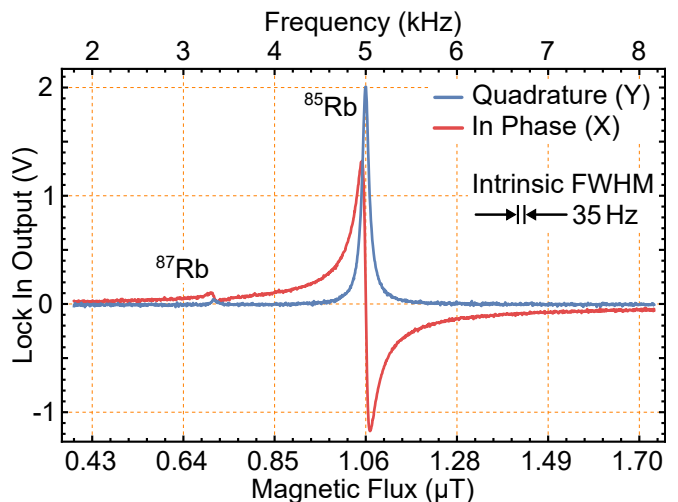


FIG. 7. In-phase X and quadrature Y component of the lock-in output for the 45° M_x -magnetometer at an incoming laser power of $5 \mu\text{W}$. A small magnetic radio frequency field B_1 was applied at 5 kHz with root-mean-square (rms) amplitude of 0.012 mA . The B_0 field was scanned across the resonance from 0 to $1.9 \mu\text{T}$ within 10 sec. A lock-in with time constant of $100 \mu\text{s}$ and 10 mV sensitivity was used.

The spin coherence lifetime and the measured linewidth above provide a first insight into the achievable sensitivity. A change of the Larmor frequency in proximity to the described frequency of $\omega_0 = 2\pi \times 5 \text{ kHz}$ does not degrade or change the signal and the derived linewidth.

A quick check of the operation at different frequencies allows for a quick visualizing of the linewidth, since it can be read off the graph directly. A magnetometer operation on different Larmor frequencies in 100 Hz steps is presented in Fig. 8.

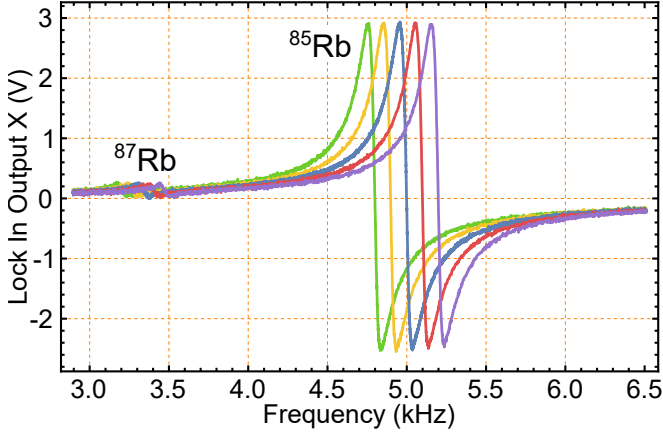


FIG. 8. In-phase lock-in output (X) for a B_0 scan at different fixed B_1 frequencies (4.8-5.2 kHz) with step size of 100 Hz. Same parameters as Fig. 7. Only the right hand side of the the B_0 sweep is shown. The opposite side is essentially equal.

The other important parameter for the sensitivity is the signal-to-noise ratio (SNR) of the acquired signal. To estimate the SNR, a measurement is performed in which the alkali atoms are driven coherently in resonance with the Larmor frequency ω_L , which is set by the static magnetic field B_0 . The photo-diode signal is acquired over a time span of 1 sec. Therefore, the unit $\sqrt{\text{Hz}}$ of the SNR is omitted in the following. The spectral density (Fig. 9) is calculated using a Hanning window. The power spectral density was integrated over the width of 3 Hz of the signal-peak (here at 5 kHz). The root mean square (rms) value times $\sqrt{2}$ gives the amplitude in Volt (V). Since the high frequency noise levels (Noise_∞) are significantly smaller than the low frequency noise levels (Noise_{lf}), we have estimated two signal-to-noise ratios. For the SNR_{lf} we chose the Noise_{lf} in immediate proximity to the signal-peak by averaging the noise floor between the signal-peak and the 50 Hz side-peak of the power line from 4960 to 4995 Hz, as indicated in Fig. 9. This noise level consist of low-frequency components caused by magnetic field fluctuations around the signal-peak. For SNR_∞ the noise Noise_∞ is used, corresponding to the average noise level between 41 and 44 kHz.

The full sensitivity of the magnetometer is a combination of the experimental values derived above. It is calculated as

$$\delta B = \frac{\Delta\nu_{\text{HWHM}}}{\gamma \cdot \text{SNR}} \quad (6)$$

with the gyromagnetic ratio γ .

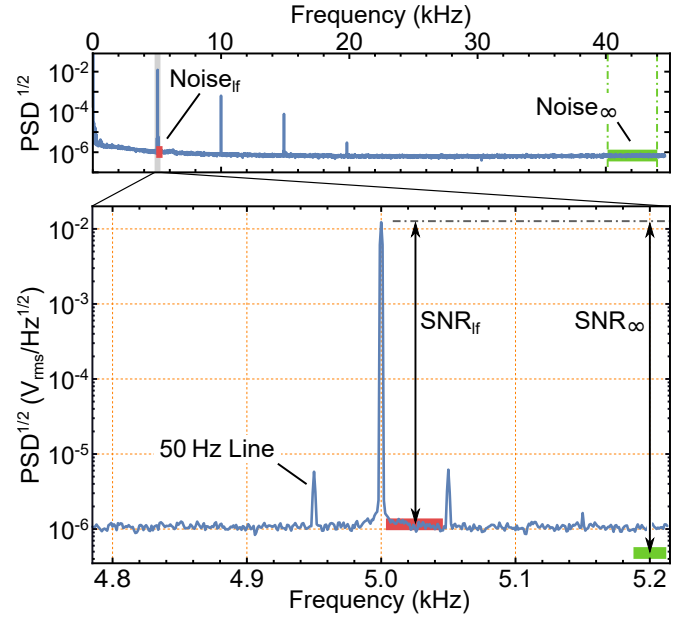


FIG. 9. Square root of the power spectral density ($\text{PSD}^{1/2}$) in free running mode. The average of 45 spectral densities convoluted with a Hanning window function is shown, each resulting from a measurement with 1 sec integration time, thus presenting the noise level for a 1 sec measurement time. The measurement was performed at an incoming laser power of 100 μW , a B_1 rms amplitude of 0.58 mA and a frequency of 5 kHz with correspondingly resonant static B_0 field. Typical 50 and 150 Hz side-peaks are due to noise at the power line frequency. Technical low frequency noise, possibly introduced by laser power fluctuations, imperfectly polarized light, and magnetic field fluctuations¹¹ increases the noise around the peak. The average low frequency noise is represented by the red bar. The signal-to-noise ratio SNR_{lf} refers to this noise level. Considering the decreased noise level at higher frequencies yields the SNR_∞ . We estimated the high-frequency noise by averaging over the frequency range between 41 – 44 kHz (green bar).

With the aforementioned described measurements, the sensitivity for our setup is calculated to $\delta B_\infty = 0.6 \text{ pT}/\sqrt{\text{Hz}}$ at an incoming laser power of 0.125 mW. δB_∞ is determined using the SNR_∞ of 39700, a width $\Delta\nu_{\text{HWHM}}$ of 111 Hz, and $\gamma = 4.7 \text{ Hz/nT}$. A second sensitivity δB_{lf} is determined referring to the SNR_{lf} . For this sensitivity, our optimum δB_{lf} of 1.5 $\text{pT}/\sqrt{\text{Hz}}$ was found at an incoming laser power of 0.05 mW, resulting in an SNR_{lf} of 12800 and a width $\Delta\nu_{\text{HWHM}}$ of 88 Hz. These values are derived from the optimization process which is described in the following.

IV. OPTIMIZATION

As described above, the sensitivity is determined by an interplay between the magnetic resonance HWHM and the SNR. The best magnetometer sensitivity is obtained at the smallest ratio between them. A variety of effects

influence these parameters. Examples are the number of polarized (pumped) atoms, the coherence of the Larmor precession between the single atoms, the influence of the rf B_1 field, magnetic field-inhomogeneities, noise etc.. All these (internal) influences are summarized in the linewidth and the signal-to-noise ratio. In the following, we present an optimization routine to achieve the highest sensitivity of the magnetometer configuration. Although there are more parameters which in principle can be taken into account (beam-diameter, density of the vapor). A change of the most evident parameters is presented. The best sensitivity dependent on the power of the rf B_1 field, and the incoming laser power is determined below.

The linewidth $\Delta\nu_{\text{HWHM}}$ of the phase signal Θ , which has been introduced above, is immune to rf B_1 power broadening for a wide range. Hence, only the laser power dependence of $\Delta\nu_{\text{HWHM}}$ is measured. The data is shown in Fig. 10. The data points of the phase Θ are fitted by Eqn. 7 and an additional linear term²².

$$\Delta\nu_{\text{HWHM}}(P_1) = \frac{\nu_{\text{sat}} \cdot P_1}{(P_{\text{sat}} + P_1)} + \nu_0 \quad (7)$$

P_1 denotes the incoming laser power, P_{sat} is a saturation power and ν_0 the width at zero power (or the cell's intrinsic linewidth), and ν_{sat} the saturation width.

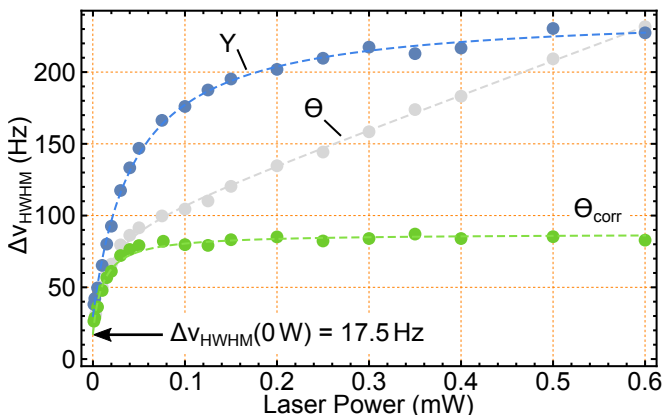


FIG. 10. Cell's linewidth (HWHM) over input laser power. The blue dots represent the linewidth of the quadrature output (Y) of the lock-in estimated by a Lorentzian fit. Fitting by Eqn. 7 yields the blue dashed line. The gray dots result from a cyclometric function fit to the phase signal Θ (cf. Fig. 6). Even though Θ excludes B_1 power broadening, we still see an artificial linear broadening which might be originated in an increasing technical noise, magnetic field fluctuations or light power broadening. The dashed gray line is a fit using Eqn. 7 with an additional linear term. Subtracting the latter yields a corrected dataset Θ_{corr} without linear broadening effects (green dots). The black arrow indicates the intrinsic linewidth at zero power, extrapolated over the fit of Θ_{corr} .

As a second step, a measurement over the power of the rf B_1 field versus the related SNRs is performed at an arbitrary constant laser power (cf. Fig. 11). The power of

the B_1 field is changed until a clear maximum SNR appears. The SNRs are estimated from the PSD (cf. Fig. 9) as mentioned above. Based on these measurements, the rf B_1 field power of the best SNR is taken to perform a further measurement sequence in which the power dependence of the SNRs is evaluated.

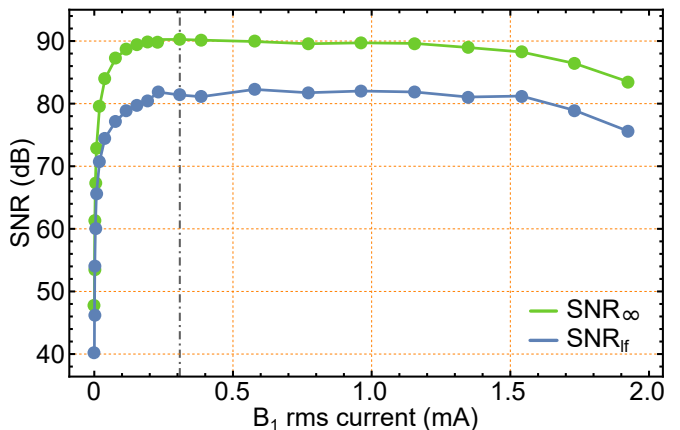


FIG. 11. Dependence of the SNR on the rms current of the rf B_1 -coil with a fixed frequency equivalent to the Larmor frequency ω_L of 5 kHz, which is set by a static magnetic field (B_0). The SNR_∞ (green line) is estimated by the noise average from 41 to 44 kHz. The blue line shows the SNR_{rf} with a noise average from 5 to 40 Hz away from the carrier (cf. Fig. 9). The gray line indicates the best SNR with a B_1 rms current of 0.31 mA. The measurement was performed at an incoming laser power of 100 μW .

The same measurements are performed as before, with the exception of changing laser power while keeping the power of the rf B_1 field constant. It should be noted, that the gain settings of the photo diode were not changed from 30 dB in the course of the measurement, since different gain settings imply a different noise level. The result of the measurements is shown in Fig. 12.

The both measurement sequences over the laser power of the $\Delta\nu_{\text{HWHM}}$ (Fig. 10) and the SNR (Fig. 12) allows a determination the related sensitivities with Eqn. 6. The obtained curves in Fig. 13 exhibit minima for the best sensitivity. It should be mentioned that in case of a sufficient time capacity, a more accurate optimization can be performed by a two-dimensional-series approach with the B_1 -amplitude, and the laser power.

V. CONCLUSION & OUTLOOK

In conclusion, we have presented and characterized a compact and simple M_x -magnetometer based on atomic rubidium. A focus was given to a special cell design, which features an anti-relaxation coating, and neon buffer gas. In terms of magnetometer sensitivity, the cells fail to perform at the level compared to when they were first produced one year ago. Additionally, they are 10-100 \times less sensitive to comparable cell describes in

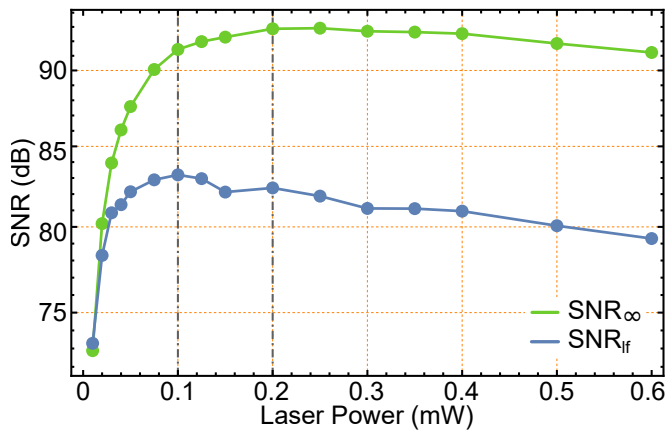


FIG. 12. Dependence of the SNR on the incoming laser power with a B_1 coil rms current of 0.31 mA, corresponding to the measurement shown in Fig. 11. The B_1 frequency was set to 5 kHz, in accordance to the Larmor frequency induced by the static B_0 -field. The maxima are located at laser powers of 0.1 mW and 0.2 mW, respectively, as indicated by the gray dashed lines.

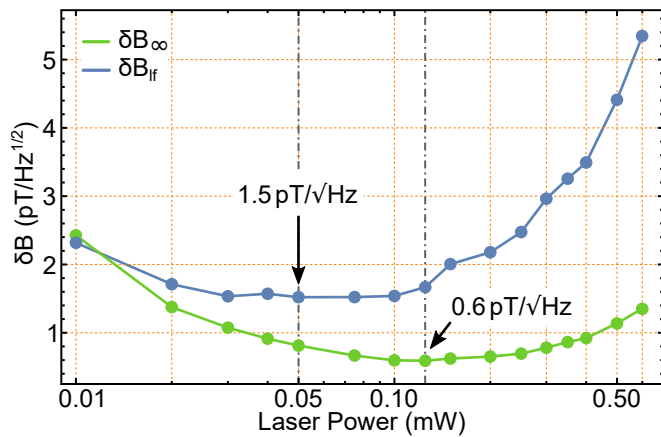


FIG. 13. Power dependence of the magnetometer's sensitivity δB determined by Eqn. 6 and the data shown in Fig. 10 and Fig. 12. We used the width of the phase signals Θ from Fig. 10 since it excludes B_1 power broadening. δB_∞ (green line) and δB_{if} correspond to the signal-to-noise ratios shown in Fig. 12 with their best sensitivities of 1.5 and 0.6 $\text{pT}/\sqrt{\text{Hz}}$ at 0.05 and 0.125 mW laser power, respectively.

literature²³. On the other hand, typically cell designs are larger and do not incorporate any collision enhancing glass features, such as the appendix, which can host a solid state sample.

The magnetometer's sensitivity is determined to be 0.6 $\text{pT}/\sqrt{\text{Hz}}$. This is based on an independent estimation of the Larmor spin precession linewidth and the achievable signal-to-noise ratio in our experimental configuration. Since the SNR was determined in a free-running magnetometer configuration, we believe that it will be possible to suppress the low-frequency noise components even more. The magnetometer's performance is characterized in slow B_0 -scans and in 1 sec time-series record-

ings. With regard to the experimental equipment the photo-diode configuration for the measurement is not ideal, and we experienced different noise levels for different amplification ratios. A photo-diode design based on a sensitive transimpedance amplifier (DLPCA-200, Femto GmbH) will be implemented in the future. Another important improvement is the in-house design of a low-noise current source, which targets the 10^{-7} relative accuracy regime with a maximum range of a few mA. For the compensation of field gradients, we will divide the (pseudo-)Helmholtz coil pairs into independent coils, which are then independently driven by current drivers.

The magnetometer is prepared to be combined with solid state spin samples. A small appendix (\varnothing 2 mm, 10 mm depth) with sub-mm thick walls can host another experiment. At present, we have prepared an optically shielded, fiber-coupled nitrogen-vacancy ensemble with a microwave loop antenna, which can be inserted into the appendix. Earlier designs featuring a hole through the entire glass cell, were not pursued further, but may eventually allow for the application with liquid samples⁴. For these combination experiments, the implementation of a light-driven Larmor precession (Bell-Bloom type²⁴) will allow for exciting the atomic spin ensemble completely independent of the solid-state sample.

ACKNOWLEDGMENTS

The authors thank the atomic physics group in Fribourg, Switzerland for their strong support and transfer of knowledge. To name is the support not only from A. Weis, but also from V. Lebedev, and Z. Grujic. Special thanks go to R. Jiménez Martínez from the Mitchell group at the ICFO in Barcelona, Spain for sharing his knowledge and hands on experience. M. Mitchell is acknowledged for his hospitality in his group. Helmut Kammerlander is strongly acknowledged for the production of the high quality glass cells used in this study. We acknowledge the work performed by S. Lasse. We further acknowledge the funding from the MPG via a Max Planck fellowship (J.W.), the SFB project CO.CO.-MAT/TR21, the Bundesministerium für Bildung und Forschung (BMBF), the project Q.COM, and SQUTEC. Lastly, D. Arnold enjoyed support from the COST action MP1403 – Nanoscale Quantum Optics.

¹Y. Zhang, Y. Tavrín, H.-J. Krause, H. Bousack, A. Braginski, U. Kalberkamp, U. Matzander, M. Burghoff, and L. Trahms, *Applied Superconductivity* **3**, 367 (1995), electronic Applications of High Temperature Superconductors.

²H. Becker, *Archaeological Prospection* **2**, 217 (1995).

³G. Bison, R. Wynands, and A. Weis, *Applied Physics B* **76**, 325 (2003).

⁴M. Ledbetter, C. Crawford, A. Pines, D. Wemmer, S. Knappe, J. Kitching, and D. Budker, *Journal of Magnetic Resonance* **199**, 25 (2009).

⁵A. Weis and R. Wynands, *Optics and Lasers in Engineering* **43**, 387 (2005), optics in Switzerland.

⁶E. S. E. H. G. Robinson and H. G. Dehmelt, *Bull. Am. Phys. Soc.* **3**, 9 (1958).

- ⁷D. Budker and M. Romalis, *Nat Phys* **3**, 227 (2007).
- ⁸I. K. Kominis, T. W. Kornack, J. C. Allred, and M. V. Romalis, *Nature* **422**, 596 (2003).
- ⁹A. Gruber, A. Dräbenstedt, C. Tietz, L. Fleury, J. Wrachtrup, and C. v. Borczyskowski, *Science* **276**, 2012 (1997), <http://science.sciencemag.org/content/276/5321/2012.full.pdf>.
- ¹⁰Y. Kubo, F. R. Ong, P. Bertet, D. Vion, V. Jacques, D. Zheng, A. Dréau, J.-F. Roch, A. Auffeves, F. Jelezko, J. Wrachtrup, M. F. Barthe, P. Bergonzo, and D. Esteve, *Phys. Rev. Lett.* **105**, 140502 (2010).
- ¹¹D. Budker and D. Kimball, *Optical Magnetometry*, Optical Magnetometry (Cambridge University Press, 2013).
- ¹²S. Groeger, G. Bison, J.-L. Schenker, R. Wynands, and A. Weis, *The European Physical Journal D - Atomic, Molecular, Optical and Plasma Physics* **38**, 239 (2006).
- ¹³D. A. Steck, Report (2013).
- ¹⁴M. V. Balabas, T. Karaulanov, M. P. Ledbetter, and D. Budker, *Phys. Rev. Lett.* **105**, 070801 (2010).
- ¹⁵W. Franzen, *Phys. Rev.* **115**, 850 (1959).
- ¹⁶A. Corney, *Atomic and Laser Spectroscopy*, Oxford Classic Texts in the Physical Sciences (OUP Oxford, 2006).
- ¹⁷S. J. Seltzer, D. M. Rampulla, S. Rivillon-Amy, Y. J. Chabal, S. L. Bernasek, and M. V. Romalis, *Journal of Applied Physics* **104**, 103116 (2008).
- ¹⁸W. Hanle, *Zeitschrift fuer Physik* **30**, 93 (1924).
- ¹⁹N. Castagna and A. Weis, *Phys. Rev. A* **84**, 053421 (2011).
- ²⁰S. J. Seltzer, *Developments in Alkali-Metal Atomic Magnetometry*, Ph.D. thesis, Faculty of Princeton University in Candidacy for The Degree of Doctor of Philosophy (2008).
- ²¹W. Demtröder, *Experimentalphysik 3: Atome, Moleküle und Festkörper*, Experimentalphysik / Wolfgang Demtröder (Springer, 2005).
- ²²S. Appelt, A. Ben-Amar Baranga, A. R. Young, and W. Happer, *Phys. Rev. A* **59**, 2078 (1999).
- ²³S. J. Seltzer and M. V. Romalis, *Journal of Applied Physics* **106**, 114905 (2009).
- ²⁴W. E. Bell and A. L. Bloom, *Phys. Rev. Lett.* **6**, 280 (1961).